Electronic structure of $CeNi_2Ge_2$ investigated by angle-resolved photoemission and density-functional calculations

D. Ehm, F. Reinert,* G. Nicolay, S. Schmidt, and S. Hüfner
Universität des Saarlandes, Fachrichtung 7.2, Experimentalphysik, 66041 Saarbrücken, Germany

R. Claessen and V. Eyert
Institut für Physik, Universität Augsburg, 86135 Augsburg, Germany

C. Geibel
Max-Planck Institut for Chemical Physics of Solids Dresden, 01187 Dresden, Germany
(Received 4 May 2001; revised manuscript received 17 August 2001; published 8 November 2001)

We present a detailed investigation of the electronic band structure of the heavy Fermion compound $CeNi_2Ge_2$ by means of angle resolved photoemission spectroscopy (ARPES). Measured with high angular and energy resolution, the experimental data from the (001) surface display several narrow bands close to the Fermi energy. The nature of these bands was identified by a comparison with augmented spherical wave (ASW) band structure calculations based on density functional theory (DFT) in the local density approximation (LDA). In contrast to the results of previous photoemission measurements on *in situ* prepared films of $CeNi_2Ge_2$ we demonstrate that the investigated bands show strong dispersion, in agreement with the theoretical results. In addition we show that the orbital character of the states close to the Fermi level is mainly Ni $3d$ and that an ''unusual giant Kondo resonance'' does not exist in the photoemission spectra.

DOI: 10.1103/PhysRevB.64.235104 PACS number(s): 71.20.Eh, 71.27.+a, 71.28.+d, 79.60.−i

I. INTRODUCTION

Strong electron–electron correlations in solids are responsible for a variety of interesting physical properties in many transition metal and rare earth compounds.[1–4] Especially the so-called heavy fermion (HF) behavior of metallic $4f$ and $5f$ compounds—where one can observe an enormous effective mass enhancement in the thermodynamic properties at low temperatures—has attracted much interest during the last two decades. If there is no magnetic ordering, most of these compounds can be described in the framework of the Fermi-liquid (FL) theory, where the hybridization of the conduction electrons with the strongly correlated f states forms heavy quasiparticles with an effective mass m^* up to the order of $m^*/m \approx 1000$ ($m =$ free electron mass). However, there exist intermetallic systems which, despite the lack of magnetic order, exhibit strong deviations from the HF-FL behavior. For example, the electrical resistivity $\rho(T)$ and the specific heat $C(T)$ of $CeNi_2Ge_2$ deviate significantly from the predictions of the HF-FL scenario, although no magnetic ordering could be observed in this system.[5] The origin of these so-called non-Fermi-liquid (NFL) effects are not completely clear, but in the case of undoped $CeNi_2Ge_2$ it is assumed that the reason for the NFL behavior is the proximity of an anitferromagnetic quantum critical point.[6,7]

In general cerium compounds have been widely studied by various techniques[8–14] because there is only one $4f$ electron ($n_f \lesssim 1$), an important fact that simplifies the theoretical description in comparison to systems with higher $4f$ occupation numbers. In principle, the most direct information on the electronic states of a solid can be obtained by angule-resolved photoemission spectroscopy (ARPES). In the context of the HF or NFL effects, which appear on the temperature and energy scale of only ≈ 1 K, the experimental limitations of ARPES are given by the finite energy resolution and the minimum sample temperatures, which are typically one or two orders of magnitude above the low-temperature regime where the coherent many-body properties of the HF system develop. However, ARPES is able to give important information on the spectral properties of HF compounds and the nature of the electronic states, especially in combination with theoretical calculations.

The quality of the investigated sample surface is important for reliable ARPES experiments: contamination, surface roughness, and disorder can strongly influence the experimental results. Although *in situ* cleaved single crystals are known to yield well ordered and contamination free surfaces, there are only a few ARPES experiments on single-crystalline Ce compounds in the literature,[15,16] mainly because of the restricted availability of such crystals and problems in the *in situ* cleavage procedure. In the particular case of $CeNi_2Ge_2$, the only published ARPES measurements[17–22] have been performed on *in situ* prepared, epitaxially grown films in different orientations.

One of the most important methods to investigate the electronic structure of solids theoretically are band structure calculations based on the density-functional theory (DFT). However, one has to bear in mind that DFT methods have well known limitations: (i) DFT is a ground state theory and does not necessarily describe the high energy excitations of the photoemission process, and (ii) the single particle energies obtained from the Kohn–Sham equations have, strictly speaking, no clear physical meaning, except for the highest occupied one, which corresponds to the ionization energy. Therefore a one-to-one correspondence to the experimental ARPES data can not be *a priori* guaranteed. Despite these

more fundamental limitations, experience has shown surprisingly good agreement between ARPES results and calculated bands in numerous cases.[23] While this has been widely accepted, it is still a matter of debate to what extent band theory can be applied to the description of *f* electron systems, where electronic correlations are important.[24] In addition to pure local density approximation (LDA) treatments (see, e.g., Refs. 25 and 26 and the review by Norman and Koelling[27])—''renormalized band'' approaches have been successful in calculating Fermi surfaces of a variety of HF systems.[24,28] Starting out from an LDA calculation ''renormalized band theory'' is based on the assumption that in a spherical harmonics expansion only the scattering phase shift associated with the *f* channel deviates substantially from the one originating from an LDA calculation, while all other phase shifts are well described by the LDA. There remains one single unknown parameter, the *f* electron phase shift, which is usually adapted to experimental data. Reversing this argument, as long as one is not particularly interested in describing the electronic correlations coming with the *f* states, an LDA treatment is justified especially for a description of the Fermi surface topology.

In this paper we present high-resolution ARPES measurements on the (001) surface of *in situ* cleaved single crystals of $CeNi_2Ge_2$. In contrast to earlier results[18,20] our low-temperature data ($T \approx 20$ K) exhibit strongly dispersing bands, which are in agreement with the results of a comprehensive band structure calculation. In addition, electronic structure theory allows the determination of the orbital character of the individual experimentally observed bands. Close to the Fermi level one can distinguish two independent features with high spectral intensity, where one peak can be assigned to the nondispersive Kondo resonance and a second one has mainly Ni $3d$ character with a narrow parabolic dispersion.

The manuscript is organized as follows: the crystal structure and sample preparation are described in the following section; the principles of the band structure calculation and the photoemission process are discussed in Sec. III, followed by a description of the experimental setup in Sec. IV. Finally, in Sec. V we present and discuss the experimental and theoretical results.

II. CRYSTAL STRUCTURE

$CeNi_2Ge_2$ belongs to a wide class of cerium compounds[12,15,25,29–31] that crystallize in the $ThCr_2Si_2$ structure having a body-centered tetragonal lattice with space group $I4/mmm$ (D_{4h}^{17}).[11] The corresponding simple tetragonal unit cell, marked by thin solid lines in Fig. 1, comprises two formula units. While the Ce atoms are located at the Wyckoff position (2a): (0,0,0), the Ni and Ge atoms are found at positions (4d): $(0,\frac{1}{2},\pm\frac{1}{4})$ and (4e): $(0,0,z_{\mathrm{Ge}})$, respectively. z_{Ge} is the positional parameter for the Ge atoms. As is evident from Fig. 1, the atoms form horizontal planes, i.e., perpendicular to the z axis at $z=0$, $z=\frac{1}{2}-z_{\mathrm{Ge}}$, $z=\frac{1}{4}$, $z=z_{\mathrm{Ge}}$, and $z=\frac{1}{2}$, with the sequence (Ce, Ge, Ni, Ge, Ce). The Ni atoms are tetrahedrally coordinated by both the Ce and Ge atoms. We extracted $z_{\mathrm{Ge}}=0.372$ from Knebel's graphical representation,[32] which is slightly different from Yamagami's[26] value where $z_{\mathrm{Ge}}=3/8$ was chosen. According to our x-ray diffraction data, the lattice constants are $a=4.153$ Å and $c=9.853$ Å. These values are in close agreement with those from other authors.[11,26,32]

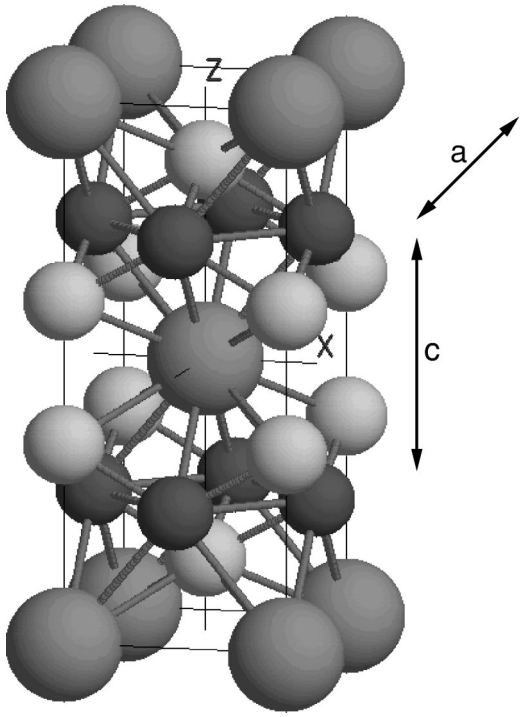

FIG. 1. Crystal structure of $CeNi_2Ge_2$ (bct). Ce, Ni, and Ge atoms are printed in medium, dark, and light gray, respectively. *x* and *z* indicate the crystal axes; *a* and *c* are the lattice constants in the respective directions.

The $CeNi_2Ge_2$ samples investigated in the present work were cut from a single crystal grown by the Czochralski technique in a Tri–Arc furnace from a slightly Ce-rich melt. Single crystals of approximately 5 mm diameter and 10 mm length were characterized and oriented using x-ray diffraction techniques. Rocking curves showed only one sharp peak. Powder x-ray patterns taken from different parts of the crystal showed only the peaks of the $ThCr_2Si_2$ structure. After orientation by Laue diffraction, the crystal was cut into slices of 1 mm thickness with the *c* axis normal to the surface.

Prior to the PES measurements the surface was prepared by *in situ* cleaving of the individual crystals at $T \lesssim 20$ K, because it was found that surface degradation of rare earth compounds is much slower at low temperature.[33] The surface quality of the sample was repeatedly controlled both by core level photoemission (XPS), which in our case showed no carbon or oxygen contamination, and by ultraviolet photoemission (UPS) in the valence band region above 7 eV, where no additional oxygen peaks could be observed.[34,35] The single crystallinity of the surface was checked by low-energy electron diffraction (LEED). A typical LEED pattern ($E_0=142$ eV) from a cleaved surface is shown in Fig. 2. Clearly visible is the fourfold symmetry and the two equiva-

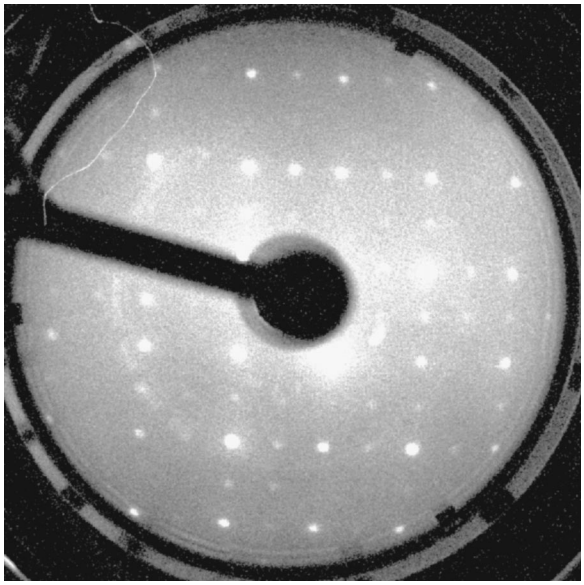

FIG. 2. LEED pattern ($E_0 = 142$ eV) of a freshly cleaved $CeNi_2Ge_2$ (001) surface (2×2 reconstructed), before being rotated to correct orientation.

lent high symmetry directions [100] and [010] in the surface plane.

III. THEORY

Our band structure calculation is based on density-functional theory (DFT) in the local density approximation (LDA).[36,37] We employ the augmented spherical wave (ASW) method[38] in its scalar-relativistic implementation (see Refs. 39–41 for more recent descriptions), which has already been used in the calculations by Sticht *et al.*[42] on $CeCu_2Si_2$ as well as for the isostructural actinide series UT_2Ge_2 (T =Mn, Fe, Co, Ni, Cu).[43] In order to minimize the sphere overlap coming with the atomic sphere approximation (ASA)[44] we used the recently developed sphere geometry optimization (SGO) method, which solves the problem of finding optimal sphere radii automatically.[45] The atomic sphere radii used in the calculations are listed in Table I, together with the basis set orbitals. States given in parentheses were included as tails of other orbitals (see Refs. 38–41 for more details on the ASW method).

Self-consistency was achieved by an efficient algorithm for convergence acceleration.[46] The Brillouin zone sampling was done using an increased number of k points ranging from 28 to 1984 points within the irreducible wedge of the tetragonal lattice, ensuring convergence of our results with respect to the fineness of the k-space grid.

TABLE I. Atomic sphere radii and basis set orbitals for $CeNi_2Ge_2$ (a_B is the Bohr radius).

Atom	Radius (units of a_B)	Orbitals				
Ce	3.907	$6s$	$6p$	$5d$	$4f$	$(5f)$
Ni	2.667	$4s$	$4p$	$3d$	$(4f)$	
Ge	2.698	$4s$	$4p$	$3d$	$(4f)$	

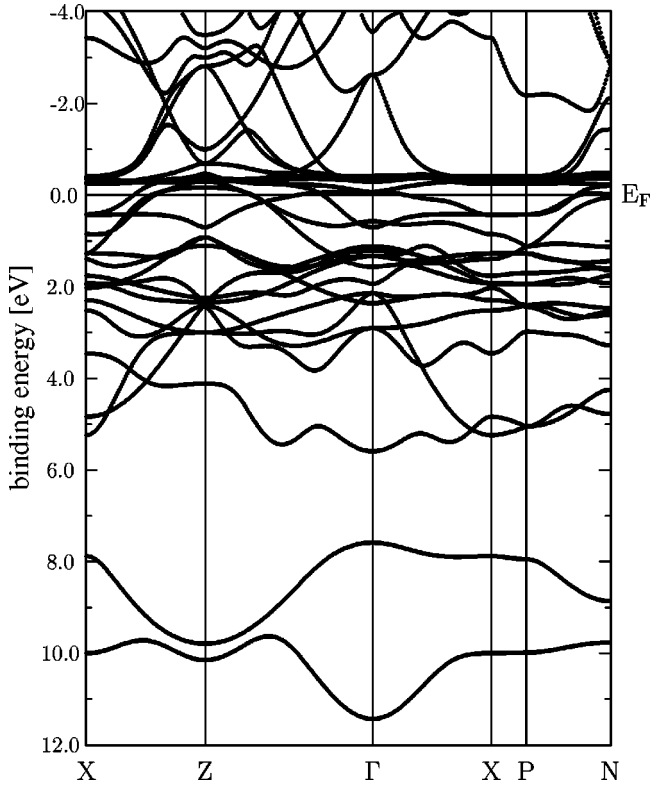

FIG. 3. Electronic bands of $CeNi_2Ge_2$ along selected symmetry lines within the first Brillouin zone of the centered tetragonal lattice (cf. Fig. 4).

Figure 3 displays the electronic states along selected high symmetry lines within the first Brillouin zone of the centered tetragonal lattice, which is shown in Fig. 4. The corresponding dominant partial densities of states (DOS) are given in Fig. 5. All other states play only a minor role in the energy interval displayed. At lower energies, we find at $E_B \approx 25$ eV the Ge $3d$ states (not shown). In addition, we observe in Fig. 3 two bands in the binding energy interval from 8 to 11.5 eV, which are almost exclusively of Ge $4s$ character.

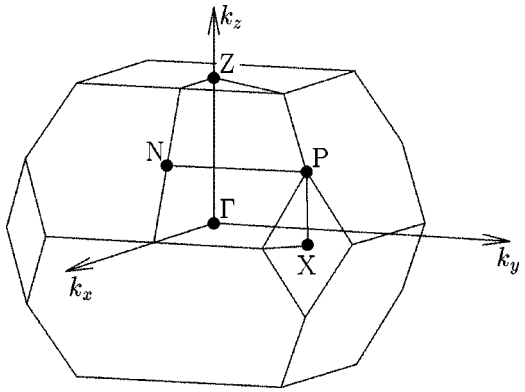

FIG. 4. Brillouin zone of the centered tetragonal structure with high-symmetry points. The photoemission data have been taken at k points in the Γ-N-Z plane. k_z is parallel to the surface normal.

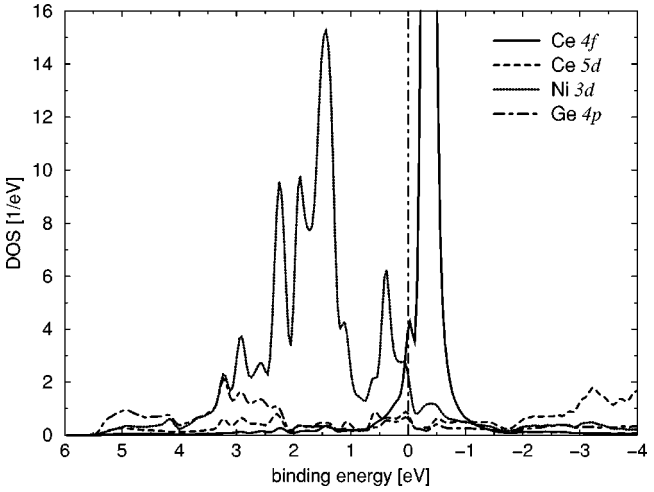

FIG. 5. Total and partial densities of states (DOS) of $CeNi_2Ge_2$ per unit cell. The maximum height of the Ce $4f$ peak amounts to 45.85 eV^{-1}.

It is obvious from the partial densities of states that the occupied part of the band structure down to binding energies of $E_B \approx 4$ eV is dominated by the Ni $3d$ states. They are accompanied by rather small contributions from the Ge $4p$ states between $E_B = 2$ eV and 4 eV. At the Fermi energy the Ce $4f$ states begin and form a strong peak at $E_B = -0.35$ eV. Finally, we observe the Ce $5d$ states above $E_B \approx -2$ eV. The change of band character near the Fermi energy from mainly Ni $3d$ to mainly Ce $4f$ is visible in more detail in Figs. 6 and 7, where we display the electronic bands in the narrow energy range from $E_B = 2.0$ eV to $E_B = -2.0$ eV in a special representation: In both figures each band at each k point is given by a bar, with a length which is a measure for the contribution from specified orbitals. According to Figs. 6 and 7 the occupied states are of mainly Ni $3d$ character. The Ni $3d$ contribution continously decreases with decreasing binding energy and becomes nearly zero at

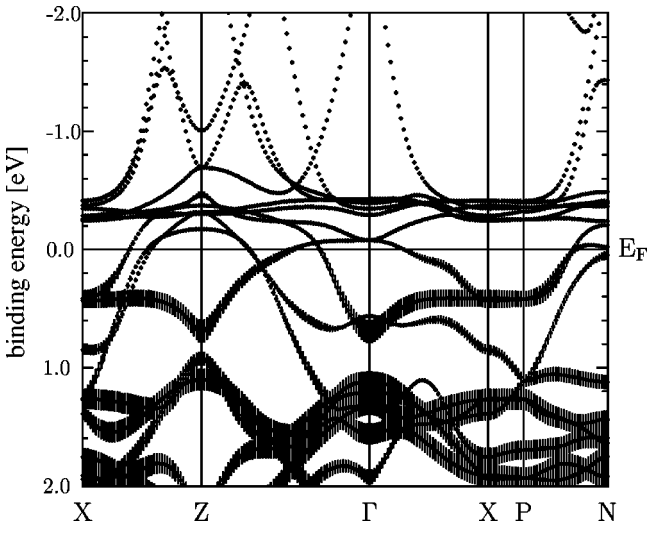

FIG. 6. Weighted electronic bands of $CeNi_2Ge_2$. The length of the vertical bars given for each k point indicates the contribution from the Ni $3d$ orbitals.

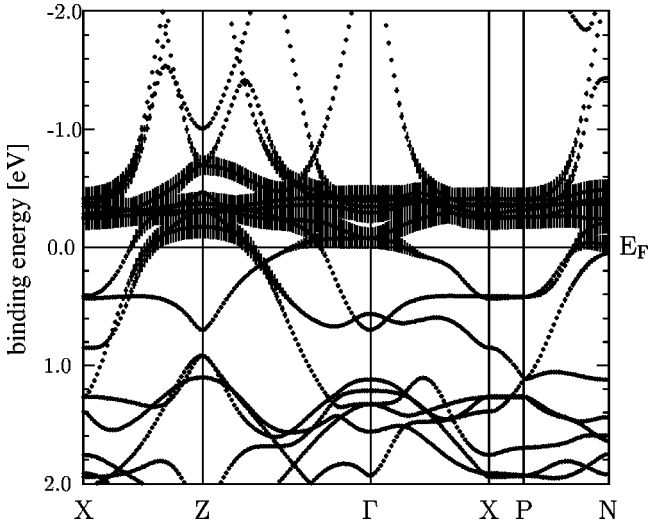

FIG. 7. Weighted electronic bands of $CeNi_2Ge_2$. The length of the vertical bars given for each k point indicates the contribution from the Ce $4f$ orbitals.

E_F, while on the other hand the Ce $4f$ character, becoming visible first at about $E_B \approx 0.4$ eV, increases rapidly in approaching the Fermi energy.

Of special interest in the subsequent analysis of the experimental data are the highest occupied bands at the Z and Γ point. According to Fig. 6 and an analysis of corresponding representations of all other orbitals, the states at $E_B = 0.64$ eV at both the Z and Γ point are of almost pure Ni $3d_{xy}$ character. In contrast, the highest occupied state at Γ, i.e., the band at $E_B = 0.58$ eV, is built up almost exclusively from the Ce $5d_{x^2-y^2}$ orbitals. All contributions of the other Ce $5d$ orbitals can be neglected in this energy and k range. In order to facilitate the following comparison with the experiment we point out that the Ce $5d_{x^2-y^2}$ and Ni $3d_{xy}$ orbitals are aligned parallel to the in-plane tetragonal axes and the diagonal of the x-y plane, respectively. With the crystal structure displayed in Fig. 1, we assign these electronic states as the in-plane σ-bonding orbitals between the respective Ni-Ni and Ce-Ce pairs neighbored within a plane.

The total density of states at the Fermi energy amounts to 8.6 states/[(formula unit) eV], corresponding to a specific heat coefficient γ of 20.3 mJ/mol K^2. This value is somewhat larger than the 16.1 mJ/mol K^2 quoted by Yamagami[26] but, as expected from an LDA-based approach, much smaller than the experimental value of 350 mJ/mol K^2.[47]

In general we find a rather good agreement of our results with those previously published by Yamagami.[26] However, there exist also distinct differences in the band structures as the splitting of the two Ge $4s$ bands at the Z point or the exact positions of the two highest occupied bands at the Γ point. In order to find the reasons for these differences we performed additional calculations with Yamagami's[26] basis set, which includes the Ce $5p$ states instead of the Ce $6p$ states, and treated the Ge $3d$ orbitals as core states. This caused significant shifts of the higher lying bands of the order of 0.2 eV. In particular, the energetic positions of the two highest occupied bands at the Γ point resembled more

the band structure published by Yamagami.[26] Nevertheless, there still remain differences, which might be due to the use of spin-orbit coupling or of the muffin–tin approximation in Yamagami's work.[26] In our calculation we find an occupation of ≈ 0.9 electrons of the Ce $6p$ states, which *a posteriori* supports our choice of basis set. Another calculation using Yamagami's[26] crystal parameters showed that the slight differences—in particular in z_{Ge}—has only little effect on the results.

In interpreting the angular dependence of the experimental photoemission spectra one must be aware of the fact that the photoelectron emission angle θ only defines the $k_{\parallel}$ component of the k vector parallel to the surface. The perpendicular component $k_{\perp}$ is not conserved at the surface and—if one assumes a free electron final state for the emitted photoelectron—can be approximately determined from the expressions

$$k_{\parallel} = \frac{\sqrt{2m}}{\hbar}\sqrt{E_{\mathrm{kin}}}\sin\theta, \tag{1}$$

$$k_{\perp} = \frac{\sqrt{2m}}{\hbar}\sqrt{E_{\mathrm{kin}}\cos^2\theta + V_0}. \tag{2}$$

Combining Eqs. (1) and (2) we obtain the component perpendicular to the surface by

$$k_{\perp} = \frac{\sqrt{2m}}{\hbar}\sqrt{E_{\mathrm{kin}} + V_0 - \frac{\hbar^2}{2m}k_{\parallel}^2}, \tag{3}$$

where m is the free electron mass. The parameters V_0 and E_{kin} are the inner potential and the kinetic energy of the photoelectrons (see Ref. 23), respectively. The kinetic energy E_{kin} depends on the binding energy of the electrons and the work function Φ_0, which defines the energetic distance between the Fermi energy and the vacuum level :

$$E_{\mathrm{kin}} = h\nu - E_B - \Phi_0. \tag{4}$$

The inner potential V_0 is related to the muffin-tin zero (MTZ), which is given by the bottom of the extended states in the LDA calculations with respect to the vacuum level:

$$V_0 = E_F - \mathrm{MTZ} + \Phi_0. \tag{5}$$

In practice, the photon energy $h\nu$ and the work function Φ_0 are specified by the experimental setup and $E_F - \mathrm{MTZ}$ is taken from the calculations.

To conclude, when performing an ARPES experiment at constant photon energy we actually follow a spherical path in k space rather than a straight line. The radius of this circle is determined by the square root of the kinetic energy E_{kin} plus the inner potential V_0. This is schematically displayed in Fig. 8 for the photon energies used in this present investigation. Here we used an inner potential $V_0 = 13.18$ eV determined from the MTZ of the band structure calculation (see above), in agreement with estimations from photon energy dependent ARPES experiments. The muffin–tin zero used was MTZ $= 8.79$ eV and the work function was set to $\Phi_0 = 4.39$ eV, which is the work function of the spectrometer and generally is similar to the one of the sample.

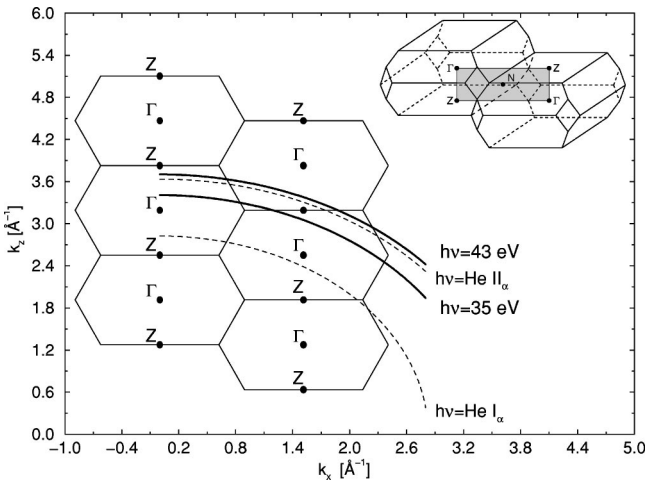

FIG. 8. Typical spherical paths through the Brillouin zone at various photon energies for states close to the Fermi level, i.e., $E_B = E_F$. The inner potential was set to $V_0 = 13.18$ eV. Upper right corner: Brillouin zone with drawn in Γ-N-Z plane (shaded area)

IV. EXPERIMENTAL SETUP

The photoemission experiments were performed on the VUV undulator beam lines U2-FSGM at BESSY I in Berlin, and BL 10.0.1 at the Advanced Light Source (ALS) in Berkeley. The crossed undulator at BESSY I, followed by a focusing spherical grating monochromator (FSGM), allowed the polarization plane of the incident light to change. The photoelectrons were analyzed with an energy resolution of $\Delta E \approx 30$ meV by an Omicron-AR 65 spectrometer, positioned on a two-axis goniometer. The 1 mm aperture of the electron lens defines an angular acceptance of $\Delta\Theta = \pm 1°$.[48] The high resolution end station at the ALS was equipped with a SCIENTA SES–200 spectrometer, which allows the photoemission spectra over an angular range of $\pm 7°$ to be measured simultaneously with an angular and energy resolution of $\Delta\Theta \approx 0.3°$ and $\Delta E \approx 11$ meV, respectively.

In both experimental setups the samples were mounted on a liquid-helium-cooled manipulator with three translational and two rotational degrees of freedom, allowing sample temperatures down to 15 K. The base pressure was below 10^{-10} mbar. The photoemission data have been measured at photon energies of $h\nu = 35$ and 43 eV, because of a reasonable photon flux of the beamlines and the high PES cross sections of the Ce $4f$ and Ni $3d$ states at these energies.[49]

V. RESULTS

Because all of the spectra presented in this paper were measured with highly polarized synchrotron radiation, we have to consider the effect of the polarization on the photoemission intensities. The left and the right panel of Fig. 9 show the energy distribution curves (EDC's) along the [100] direction (i.e., $k_{\parallel}$ lies in the Γ-N-Z plane) using an excitation energy of $h\nu = 43$ eV with s- and p-polarized light, respectively. It is obvious that especially the spectral features very close to E_F appear more pronounced in the spectra with s polarization, e.g., at an emission angle of $\Theta = 45°$. For a

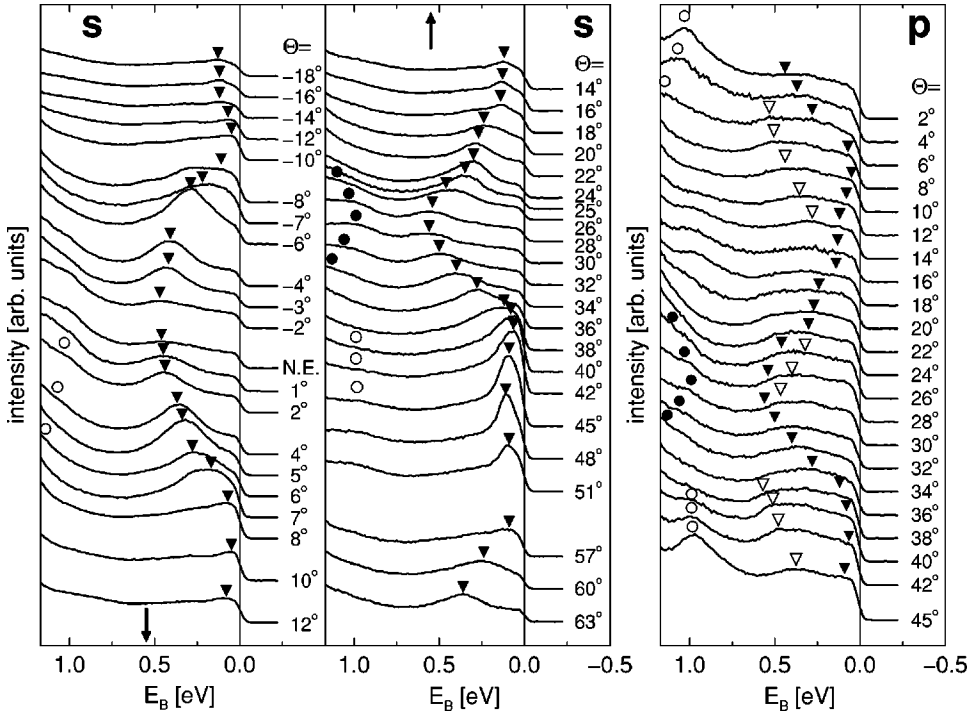

FIG. 9. Angle resolved PE spectra taken at $h\nu=43$ eV with *s*-polarized (left panel) and *p*-polarized (right panel) light at $T=15$ K in the Γ-*N*-*Z* plane by changing the polar angle Θ relative to the surface normal. The spectra are normalized to the photon flux. The triangles and circles indicate the maximum positions of the *sp* features. The filled symbols indicate the peaks found in *s* polarization; the hollow ones represent the peak positions in *p* polarization. For clarity these symbols are also copied into the respective other data set.

better comparison of the two data sets we indicate the peak positions from the EDCs in *s* polarization (left panel, labeled with filled symbols) also in the data with *p* polarization (right panel, labeled with open symbols) at the respective angles, and *vice versa*.

The dominating spectral feature in the data with *s* polarization is labeled with a filled triangle. It disperses over an energy range of nearly 500 meV with binding energy maxima at normal emission ($\Theta=0°$) and $\Theta\approx30°$. In the data measured in *p* polarization there is only little intensity from this feature. Another feature appears at higher binding energies >1 eV (circles) and near the Fermi level (open triangles).

An instructive way to display the dispersion of spectral features is to plot the second derivative $d^2I(E,k_\parallel)/dE^2$ of the individual EDC's in a gray scale plot as a function of $k_\parallel$ and binding energy (see Fig. 10). This representation is especially advantageous in comparison to the EDC's as in Fig. 9 for strongly dispersing bands. The gray scale plot—the peak maxima appear as darkened areas—allow the calculated band structure with the experimental data to be immediately compared. We have to take into account the influence of the inner potential V_0 to the theoretical description of the band structure [cf. Eq. (5)]: because V_0 cannot be determined unambiguously from the experiments, we calculate the band structure for different values of V_0 within reasonable limits. The results of these calculations are shown in Fig. 10 together with a gray scale plot for the experimental data displayed in the left panel of Fig. 9 ($h\nu=43$ eV, *s* polarization). The points at $k_\parallel=0$ represent normal emission; the center of the next nearest Brillouin zone (BZ) is close to $k_\parallel\approx1.5$ Å^{-1} (*Z* point, see Fig. 8).

For the following discussion it is useful to distinguish three of the calculated bands: band A in the energy range between the Fermi level and $E_B\approx0.7$ eV, with a binding

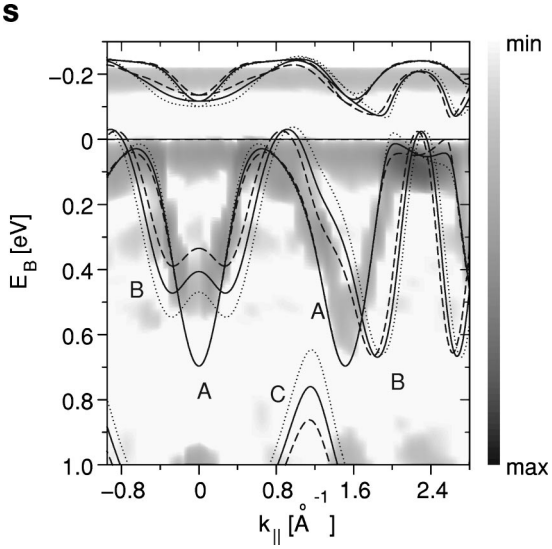

FIG. 10. Gray scale plot of the second derivative of the EDC's in *s* polarization ($h\nu=43$ eV) shown in Fig. 9, left panel. Dark structures reflects the position of peak maxima in the EDC's. The dashed, solid and dotted lines represent the LDA results using different values for the inner potential V_0, set to 12.18 eV (dashed line), 13.18 eV (solid line), and 14.18 eV (dotted line).

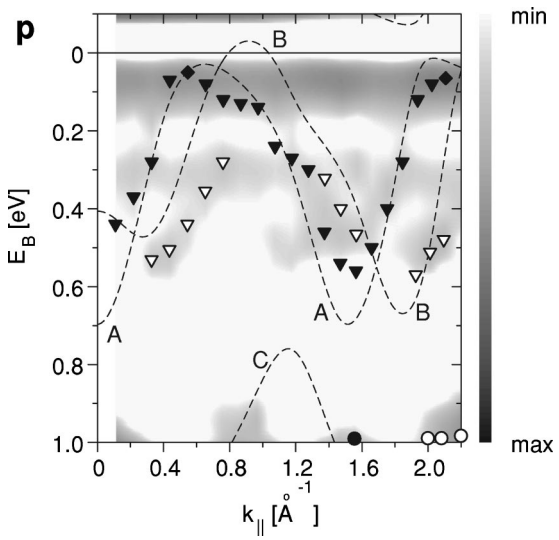

FIG. 11. Gray scale plot of the second derivative of the EDC's in p polarization ($h\nu=43$ eV) shown in Fig. 9, right panel. The dashed lines represent the LDA result with $V_0=13.18$ eV. The filled and hollow symbols are the same used in Fig. 9 to display the peak maximum positions.

energy maximum at $k_\parallel=0$ and $k_\parallel\approx1.5$ Å^{-1} and a second band B can be found in the same energy range with a W-shaped dispersion around normal emission ($k_\parallel=0$). The third band C has its minimum binding energy of $E_B=0.65$ eV to 0.85 eV around $k_\parallel=1.15$ Å^{-1}. It is obvious that all bands reveal a more or less pronounced sensitivity on the inner potential V_0: By increasing V_0 the bottom of the W-shaped part of band B moves to higher binding energies, whereas other parts of the same band show no change with V_0. The plotted part of band C shifts in opposite direction. Band A shows only slight changes at energies close to E_F.

The comparison of the calculated bands with the experimental dispersions in Fig. 10 shows an accurate agreement of the theoretical band A (at $V_0=13.18$ eV) with the main spectral feature in the s-polarized data, especially very close to E_F at $k_\parallel=2.25$ Å^{-1}. Contributions from the other two bands B and C cannot be resolved in this s-polarization data. But the gray scale plot of the spectra taken with p polarization describes a different situation (see Fig. 11). The comparison of the experimental dispersions with the theoretical bands A, B, and C (calculated with $V_0=13.18$ eV) shows that in addition to band A (filled triangles from Fig. 9) band B also (hollow triangles from Fig. 9) can be found in the experimental data.

From the theoretically known orbital character of the bands one can conclude that the observed band A results from states with mainly Ni $3d_{xy}$ character, whereas band B mostly contains contributions from the Ce $5d_{x^2-y^2}$ orbitals. If one takes into account the spatial orientation of these initial state orbitals, in respect to the experimental geometry (vector potential of the incident light, detection plane of the analyzer), and assumes that all corresponding PES final states carry mainly s character, one can calculate the matrix elements of the photoemission process. In this way it can be shown that the contribution of the Ce $5d_{x^2-y^2}$ orbitals to the photoemission intensities at s polarization will always be close to zero in our case. In contrast, we get nonzero matrix elements for photoemission in p polarization for the Ce $5d_{x^2-y^2}$ orbitals, which still depend on the emission angle Θ. The contribution of the Ni $3d_{xy}$ orbitals to the PES matrix elements should be nonzero for both polarization directions. This is in accordance with our experimental observation.

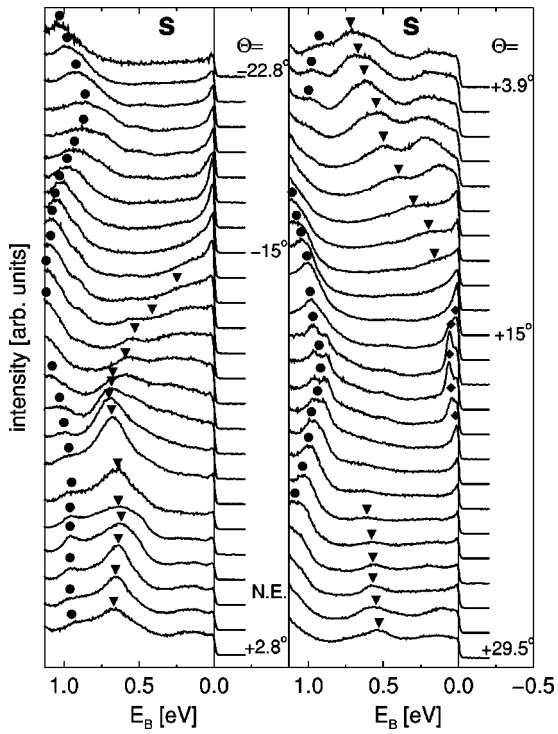

FIG. 12. Angle resolved PE spectra taken with p-polarized light ($h\nu=35$ eV) at $T=15$ K close by the Γ-N-Z plane (see Fig. 8); $\Delta E\approx11$ meV and $\Delta\theta\approx0.3°$. The spectra are normalized to the photon flux. The triangles and circles indicate the maximum positions of the peaks.

Figure 12 shows a series of EDC's measured with $h\nu=35$ eV in p polarization. To investigate the shape of the spectral features in more detail we used here a much higher energy and angular resolution than in the experiments described above, namely $\Delta E\approx11$ meV and $\Delta\Theta\approx0.3°$. In principle one can observe the same spectral features as already seen in the data in Fig. 9 measured with $h\nu=43$ eV. The differences between the spectra at the two different photon energies are due to the different k paths in the three-dimensional BZ (see Fig. 8).

Special attention should be paid to the spectral feature close to E_F that appears most distinct at emission angles around $\Theta=\pm15°$. To discuss this feature in more detail we give in Fig. 13 a magnified view of the relevant spectra from Fig. 12, both as EDCs and a gray scale plot. The peak maximum follows a parabolic dispersion with a maximum binding energy of only $E_B=70$ meV at $k_\parallel=0.87$ Å^{-1}. This is close to a Bragg plane between the first and the neighboring BZ (see Fig. 8). Within a small angular range of $\pm2°$ the peak shifts steeply towards E_F and crosses the Fermi level at $k_F\approx0.87\pm0.05$ Å^{-1}. At negative emission angles (around $\Theta=-18°$) there is also an enhanced intensity near E_F but

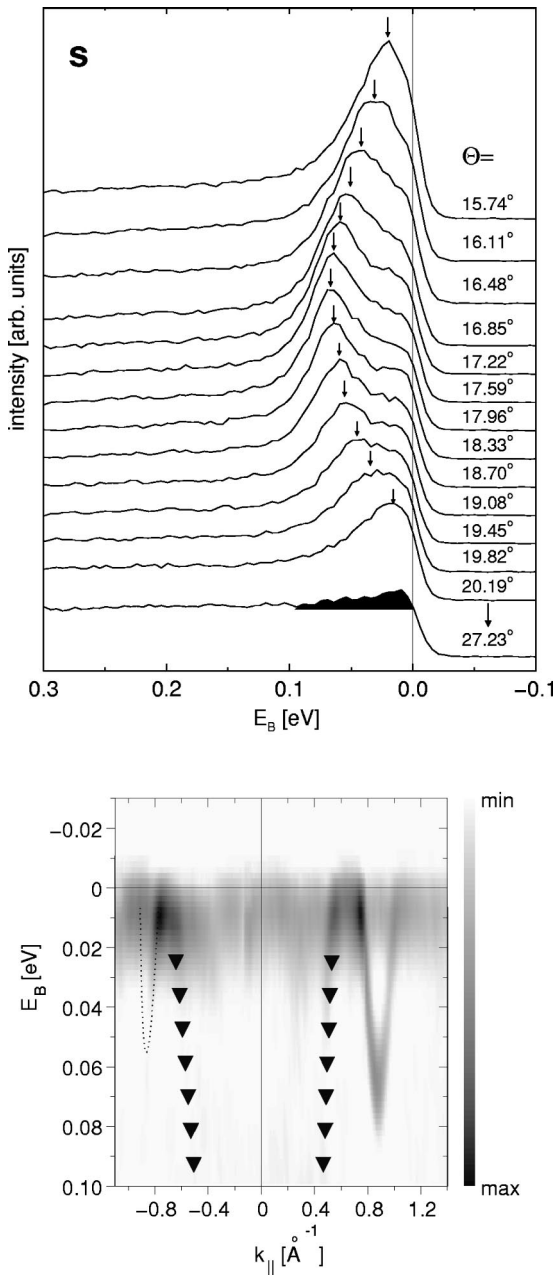

FIG. 13. Top: enlarged view of the data in Fig. 12 ($h\nu = 35$ eV); the arrows indicate the position of the main peak. Bottom: gray scale plot of the second derivative of EDC's shown above; the inserted triangles indicate the peak maximum positions of the feature already seen in the EDC's of Fig. 12, which cannot be resolved in this gray scale analysis.

we could not resolve the features with the same clarity as for positive emission angles. At a photon energy of $h\nu = 43$ eV a similar narrow band appears at emission angles around $\Theta = 45°$, corresponding to $k_{\|} = 2.3$ Å^{-1} (see Figs. 9 and 10), which in the 3–dimensional k–space is equivalent to the point where the peak appears with $h\nu = 35$ eV (see Fig. 8). From the theoretical results also given in Fig. 10 it can be seen that in this k region both band A and band B approach or even cross the Fermi level. With the inner potential $V_0 = 13.18$ eV band A exhibits a local binding energy maximum of $E_B = 0.09$ eV at $k_{\|} = 2.35$ Å^{-1}. Therefore we conclude that both spectral features at $h\nu = 35$ eV and 43 eV belong to the same band A which has predominantly Ni $3d$ character.

In addition to this dispersing Ni $3d$ peak the EDC's of Fig. 13 show also an enhanced intensity at E_F that has a weaker dependence on the emission angle than the other band features discussed so far. For example, in Fig. 12 one can clearly see that this enhanced intensity exists over a much larger angular range than the dispersing maximum, and—in principle—can be observed in all measured EDC's. To demonstrate this we added in Fig. 13 a spectrum at $\theta = 27.23°$ far off the angular range where the narrow Ni $3d$ peak appears. Obviously there exists another spectral feature close to the Fermi level, which we interpret as a *Kondo resonance* (KR), which has been observed for various polycrystalline and single-crystalline Ce compounds.[13,16,23,50–58] Angular dependent measurements on single crystalline samples showed that the spectral weight of the KR is dependent on the emission angle, whereas the peak maximum remains pinned at the Fermi level.[16] In contrast to the other experimentally observed bands, which are in good agreement with the LDA band structure, the Kondo resonance cannot be adequately described by the LDA calculation, since it is a typical many–body feature of the $4f$ spectral function.

We summarize our results as follows:

(1) In the theoretical calculations we can distinguish three bands with different orbital character. Band A and B are of mainly Ni $3d_{xy}$ and Ce $5d_{x^2-y^2}$ character, respectively. The third band C, which is positioned at higher binding energies, is of Ni $3d$ character.

(2) Band A can be immediately found in the experimental data with *s*-polarized light, whereas band B cannot be observed here. Its spectral signature appears, however, throughout comparatively weak in the data measured with *p* polarization.

(3) A narrow low-energy feature is visible close to E_F when the $k_{\|}$ component lies close to a Bragg plane between two adjacent Brillouin zones (N-N cut, cf. Fig. 8). This feature is of mainly Ni $3d$ character.

(4) Independent of this Ni $3d$ peak is a nondispersing peak at the Fermi level, which we assign to the Kondo resonance of the $4f$ spectral function.

There exist only a few angle resolved photoemission experiments on single crystalline Ce compounds in the literature.[15,16] In the case of $CeNi_2Ge_2$, photoemission experiments on epitaxially grown thin films of $CeNi_2Ge_2$ have been published.[18–21] In Refs. 18 and 20 the authors report on the preparation of a (001) surface of $CeNi_2Ge_2$, which allowed the first ARPES investigation of the band structure of this system. But the results show significant discrepancies compared to the results of the present work. Over the complete energy range the given spectra indicate only a weak angular dependence. Furthermore, at low temperature ($T = 20$ K) there appears an enhanced spectral weight close to the Fermi energy, which the authors in Ref. 18 discuss in detail as being the tail and the spin-orbit sideband of the Kondo resonance. Because the experimental band structure

shows practically no dispersion in the complete valence band range, the authors also conclude that the band structure corresponds to the dispersion of heavy quasiparticles, as known from the renormalized band structure calculation for $CeCu_2Si_2$.[42]

From our results one must infer that both conclusions can not be valid. First one should note that at low photon energies used for the experiments in Refs. 18 and 20 the photoemission cross section for the excitation of the Ce $4f$ states is nearly negligible in comparison to the cross sections for the other valence band states. Typical photon energies for the investigation of the Ce $4f$ spectra are around $h\nu = 40$ eV. However, our data measured with $h\nu = 35$ eV and $h\nu = 43$ eV show no indication of heavy Fermion bands at higher binding energies, but strongly dispersing bands as described by the LDA. Only directly at E_F do we see the slightly enhanced intensity, which we assign to the Kondo resonance. In comparison to the other spectral features—in particular the narrow Ni $3d$ peak close to E_F—the intensity of this Kondo resonance is small. But at lower photon energies the narrow Ni $3d$ peak might easily be misinterpreted as a ''giant Kondo resonance.''[18]

Another possible reason for the different experimental results might be due to the surface quality: It is known that surface degradation of rare earth systems[33] can influence the spectroscopic results significantly. Therefore all our experiments were performed on single crystals cleaved at low temperature and subsequently measured at $T < 20$ K to avoid an accelerated deterioration of the surfaces. In addition, the use of synchrotron radiation has the advantage of optimum UHV conditions without leakage gas from the discharge lamp. We tried to reduce the exposure time of the surfaces as far as possible and repeatedly checked the surface quality by measuring the spectra at higher binding energies. The binding energy range from $E_B = 4.0$ eV to 7.0 eV is extremely sensitive to an oxidation of the surface, due to the appearance of the O $2p$ features.[34,35] The spectra shown in Ref. 20 show exactly in this energy range a considerable intensity which does not exist in our data. An influence of the larger angular acceptance ($\Delta\Theta = 3°$) and energy resolution ($\Delta E = 150$ meV) alone, compared to the setup for the data presented here, cannot explain the obvious discrepancy.

VI. CONCLUSIONS

In this work we have presented high-resolution, angle-resolved photoemission measurements on $CeNi_2Ge_2$, using synchrotron radiation with changeable polarization direction. The measurements have been performed on high-quality single crystals cleaved *in situ* at low temperatures. Paying special attention to surface quality we could determine the experimental electronic band structure along certain three-dimensional paths in the Γ-N-Z plane. In contrast to previous investigations[18,20] we observe strongly dispersing bands. A comparison with new LDA band structure calculations along spherical paths in the three-dimensional BZ allows the unambiguous assignment of these experimentally observed bands to be predominantly of Ni $3d$ character. Close to the Fermi level we observe a sharp spectral feature that follows a narrow parabolalike dispersion over an energy range of 70 meV. The existence of this feature is confined to a small angular range, in contrast to an additional intensity enhancement pinned at the Fermi level, which shows only a weak dependence of spectral weight on the emission angle. Because this feature is also explained by the LDA calculation the appearance of an ''unusual giant Kondo resonance''[18] claimed in a precious study on $CeNi_2Ge_2$ could not be confirmed.

ACKNOWLEDGMENTS

This work was supported by the Bundesministerium für Bildung und Forschung (BMBF) and by the Deutsche Forschungsgemeinschaft (DFG), the Sonderforschungsbereich SFB 277 (Saarbrücken), Forschergruppe HO 955/2, and Sonderforschungsbereich SFB 484 (Augsburg). We would like to thank Z.-X. Shen, Stanford University, CA, for given us the possibility to perform the measurements at the ALS and his group members for the support at the beam line.

*Corresponding author. Email address: friedel@mx.uni-saarland.de

[1] J. Bednorz and K. A. Müller, Z. Phys. B: Condens. Matter **64**, 189 (1986).
[2] P. Lee, T. Rice, J. Serene, L. Sham, and J. Wilkins, Comments Condens. Matter Phys. **12**, 99 (1986).
[3] G. Stewart, Rev. Mod. Phys. **56**, 755 (1984).
[4] F. Steglich, J. Aarts, C. Bredl, W. Lieke, D. Meschede, W. Franz, and H. Schäfer, Phys. Rev. Lett. **43**, 1892 (1979).
[5] Z. Kletowski and M. Glinski, J. Magn. Magn. Mater. **47&48**, 524 (1985).
[6] F. Steglich, B. Buschinger, P. Gegenwart, M. Lohmann, R. Helfrich, C. Langhammer, P. Hellmann, L. Donnevert, S. Thomas, A. Link, C. Geibel, M. Lang, G. Sparn, and W. Assmus, J. Phys.: Condens. Matter **8**, 9909 (1996).
[7] F. Steglich, P. Gegenwart, C. Geibel, R. Helfrich, P. Hellmann, M. Lang, A. Link, R. Modler, G. Sparn, N. Büttgen, and A. Loidl, Physica B **223-224**, 1 (1996).
[8] P. Gegenwart, F. Kromer, M. Lang, G. Sparn, C. Geibel, and F. Steglich, Phys. Rev. Lett. **82(6)**, 1293 (1999).
[9] H.-A. Krug von Nidda, A. Schütz, M. Heil, B. Elschner, and A. Loidl, Phys. Rev. B **57**, 14 344 (1998).
[10] H. Sato, Y. Aoki, J. Urakawa, H. Sugawara, Y. Onuki, T. Fukuhara, and K. Maezawa, Phys. Rev. B **58**, 2933 (1998).
[11] T. Fukuhura, K. Maezawa, H. Ohkuni, T. Kagayama, and G. Oomi, Physica B **230-232**, 198 (1997).
[12] N. Büttgen, H.-A. Krug von Nidda, and A. Loidl, Physica B **230-232**, 590 (1997).
[13] D. Malterre, M. Grioni, and Y. Baer, Adv. Phys. **45**, 299 (1996).
[14] E. Paulus and G. Voss, J. Magn. Magn. Mater. **47&48**, 539 (1985).
[15] J. Denlinger, G.-H. Gweon, J. Allen, C. Olson, M. Maple, J. L. Sarrao, P. Armstrong, Z. Fisk, and H. Yamagami, J. Electron Spectrosc. Relat. Phenom. **117-118**, 347 (2001).
[16] M. Garnier, K. Breuer, D. Purdie, M. Hengstberger, and Y. Baer, Phys. Rev. Lett. **78**, 4127 (1997).
[17] G. Fecher, B. Schmied, A. Oelsner, and G. Schnhense, J. Electron

Spectrosc. Relat. Phenom. **114–116**, 747 (2001).
[18] G. Fecher, B. Schmied, and G. Schönhense, J. Electron Spectrosc. Relat. Phenom. **101-103**, 771 (1999).
[19] B. Schmied, M. Wilhelm, U. Kübler, M. Getzlaff, G. H. Fecher, and G. Schönhense, Physica B **230-232**, 290 (1997).
[20] B. Schmied, G. Fecher, C. Schneider, and G. Schönhense, Appl. Phys. A: Solids Surf. **66**, 385 (1998).
[21] B. Schmied, M. Wilhelm, U. Kübler, M. Getzlaff, G. H. Fecher, and G. Schönhense, Surf. Sci. **377-379**, 251 (1997).
[22] B. Schmied, M. Wilhelm, U. Kübler, M. Getzlaff, G. Fecher, and G. Schönhense, J. Am. Ceram. Soc. **358**, 141-143 (1997).
[23] S. Hüfner, *Photoelectron Spectroscopy* Vol. 82 of *Springer Series in Solid-State Sciences* (Springer-Verlag, Berlin, 1996).
[24] P. Fulde, *Electron Correlations in Molecules and Solids*, Vol. 100 of *Springer Series in Solid-State Sciences* (Springer-Verlag, Berlin, 1995).
[25] E. Runge, R. Albers, N. Christensen, and G. Zwicknagl, Phys. Rev. B **51**, 10 375 (1995).
[26] H. Yamagami, J. Phys. Soc. Jpn. **68**, 1975 (1999).
[27] M. Norman and D. Koelling, *Electronic Structure, Fermi Surfaces and Superconductivity in f Electron Metals* (North-Holland, Amsterdam, 1993), Vol. 17, Chap. 110, pp. 1–85.
[28] P. Fulde, J. Keller, and G. Zwicknagl, *Theory of Heavy Fermion Systems*, Vol. 41 of *Solid State Physics* (Academic Press, New York, 1988), pp. 1–150.
[29] S. Lister, F. Grosche, F. Carter, R. Haselwimmer, S. Saxena, N. Mathur, S. Julian, and G. Lonzarich, Z. Phys. B: Condens. Matter **103**, 263 (1997).
[30] F. Steglich, P. Gegenwart, R. Helfrich, C. Langhammer, P. Hellmann, L. Donnevert, C. Geibel, M. Lang, G. Sparn, W. Assmus, G. R. Steward, and A. Ochiai, Z. Phys. B: Condens. Matter **103**, 235 (1997).
[31] Z. Kletowski, J. Less-Common Met. **95**, 127 (1983).
[32] G. Knebel, Ph.D. thesis, Universität Augsburg (1999).
[33] F. Reinert, R. Claessen, G. Nicolay, D. Ehm, S. Hüfner, W. P. Ellis, G.-H. Gweon, J. W. Allen, and W. Aβmus, Phys. Rev. B **58**, 12 808 (1998).
[34] D. H. Ehm, Ph.D. thesis, Universität des Saarlandes (2002).
[35] M. Matsumoto, K. Soda, K. Ichikawa, S. Tanaka, Y. Taguchi, K. Jouda, O. Aita, Y. Tezuka, and S. Shin, Phys. Rev. B **50**, 11 340 (1994).
[36] P. Hohenberg and W. Kohn, Phys. Rev. **136**, B864 (1964).
[37] W. Kohn and L. J. Sham, Phys. Rev. **140**, A1133 (1965).
[38] A. R. Williams, J. Kübler, and C. D. Gelatt, Phys. Rev. B **19**, 6094 (1979).
[39] V. Eyert, Ph.D. thesis, Technische Hochschule Darmstadt (1991).
[40] J. Kübler and V. Eyert, *Electronic and Magnetic Properties of Metals and Ceramics* (VCH Verlagsgesellschaft, Weinheim, 1992), Vol. 3A, pp. 1–145.
[41] V. Eyert, Int. J. Quantum Chem. **77**, 1007 (2000), special issue: Electronic Structure of Materials.
[42] J. Sticht, N. d'Ambrumenil, and J. Kübler, Z. Phys. B: Condens. Matter **65**, 149 (1986).
[43] S. F. Matar, V. Eyert, A. Mavromaras, S. Najm, B. Chevalier, and J. Etourneau, J. Magn. Magn. Mater. **174**, 219 (1997).
[44] O. K. Andersen, Phys. Rev. B **12**, 3060 (1975).
[45] V. Eyert and K. H. Höck, Phys. Rev. B **57**, 12 727 (1998).
[46] V. Eyert, J. Chem. Phys. **124**, 271 (1996).
[47] G. Knopp, A. Loidl, R. Caspary, U. Gottwick, C. D. Bredl, H. Spille, F. Steglich, and A. P. Murani, J. Magn. Magn. Mater. **74**, 341 (1988).
[48] C. Janowitz, R. Müller, T. Plake, T. Böker, and R. Manzke, J. Electron Spectrosc. Relat. Phenom. **105**, 43 (1999).
[49] J. J. Yeh and I. Lindau, At. Data Nucl. Data Tables **32**, 1-155 (1985).
[50] A. Sekiyama, T. Iwasaki, K. Matsuda, Y. Saitoh, Y. Onuki, and S. Suga, Nature (London) **403**, 396 (2000).
[51] J.-S. Kang, C. Olson, M. Hedo, Y. Inada, E. Yamamoto, Y. Haga, Y. Onuki, S. Kwon, and B. Min, Phys. Rev. B **60**, 5348 (1999).
[52] A. Arko, J. Joyce, A. Andrews, J. Thompson, J. Smith, E. Moshopoulou, Z. Fisk, A. Menovsky, P. Canfield, and C. Olson, Physica B **230-232**, 16 (1997).
[53] J. Lawrence, A. Arko, J. Joyce, R. Blyth, R. Bartlett, P. Canfield, Z. Fisk, and P. Riseborough, Phys. Rev. B **47**, 15 460 (1993).
[54] F. Patthey, J.-M. Imer, W.-D. Schneider, H. Beck, Y. Baer, and B. Delley, Phys. Rev. B **42**, 8864 (1990).
[55] F. Patthey, W.-D. Schneider, and Y. Baer, Phys. Rev. Lett. **58**, 2810 (1987).
[56] R. Parks, S. Raaen, M. den Boer, Y.-S. Chang, and G. Williams, Phys. Rev. Lett. **52**, 2176 (1984).
[57] R. Parks, M. den Boer, S. Raaen, J. Smith, and G. Williams, Phys. Rev. B **30**, 1580 (1984).
[58] J. Lawrence, Phys. Rev. B **26**, 2362 (1982).